



Experimental and Numerical Validation of an Effective Stress-Sensitive Permeability Model Under Hydromechanical Interactions

Teng Teng^{1,3} · Zhaolong Li² · Yuming Wang² · Kun Liu² · Wenjian Jia²

Received: 9 July 2023 / Accepted: 25 November 2023 / Published online: 2 January 2024
© The Author(s), under exclusive licence to Springer Nature B.V. 2023

Abstract

Water seepage in rocks, in geotechnical engineering such as the hydrofracturing of hard rocks, excavation of underground chambers, and prevention of mine water disasters, is a common problem. According to rock mechanics theory, the deformation and stress of rocks influence seepage behavior. In this study, a modified permeability model of argillaceous sandstone under coupled hydromechanical conditions was established to reveal the relationship between permeability and effective stress, including external stress and internal water pressure. The modeling results indicate a negative exponential relationship between the argillaceous sandstone permeability and the effective stress. The proposed effective stress-sensitive permeability model was validated by conducting two sets of seepage experiments based on controlling the water pressure and external stress, with the results obtained considered satisfactory. Based on the proposed permeability model, a fully coupled multifield model of the water seepage and rock deformation was developed. Fully coupled scenario-based numerical simulations were conducted in a finite element environment to investigate water seepage evolution and rock deformation. The experimental and numerical results show that the trends in the evolution of the entire compressive stress–strain and permeability curves are reversed, and the maximum value of the permeability was not consistent with the failure of argillaceous sandstone. This model and corresponding numerical simulations can provide insights for water seepage research and serve as a reliable theoretical basis for evaluating roof water injection and hydraulic fracturing in rock and mining engineering.

✉ Teng Teng
T.Teng@cumtb.edu.cn

¹ State Key Laboratory for Geo-Mechanics and Deep Underground Engineering, China University of Mining and Technology-Beijing, Beijing 100083, China

² School of Energy and Mining Engineering, China University of Mining and Technology-Beijing, Beijing 100083, China

³ State Key Laboratory Cultivation Base for Gas Geology and Gas Control, Henan Polytechnic University, Jiaozuo 454003, China

Article Highlights

- Effective stress-sensitive permeability model was developed and validated experimentally
- Established fully coupled model of water seepage and rock deformation
- Numerical simulation revealed evolutions of the rock permeability and deformation

Keywords Permeability model · Hydromechanical interactions · Rock seepage experiment · Numerical simulation

1 Introduction

In geotechnical engineering, hydraulic fracturing, excavation of underground chambers, and roof water injection in coal mining can lead to water seepage into rocks (He et al. 2012; Lu et al. 2013; Pan et al. 2022; Kacimov et al. 2022; Fan et al. 2012). Relevant studies have been conducted on the seepage characteristics and influencing factors under coupled fluid–solid conditions (Yu et al. 2022a; Chen et al. 2022; Guo et al. 2014; Li et al. 2022) by the research means of experimental analyses, mechanical modeling, and numerical simulations.

In 1941, Biot (1941) proposed a 3D consolidation theory that formed the basis for studying the theory of the interaction between rock deformation and seepage. In 1943, the theoretical model of fluid–solid interaction was first proposed based on the effective stress principle proposed by Terzaghi (1943). Many scholars have continued to improve the theory and form a relatively complete system for studying seepage mechanics (Biot and Willis 1957). Andreas et al. (2014) developed a discrete element model (DEM) to simulate dynamic fracturing driven by the internal generation of fluids in low-permeability elastic solids by studying the effects of fluid pressure on fractured systems. Golovin and Baykin (2018) studied the effect of pore pressure on the development of hydraulically driven fractures in poroelastic media. Hadi and Homayoon (2017) introduced a new empirical model for estimating groundwater seepage based on field surveys and laboratory analyses. After determining single- and two-variable relationships with water seepage, an appropriate model for estimating the leakage was obtained using a stepwise algorithm. Wen et al. (2018) analyzed the hydraulic fracturing mechanism and cracking form in coal rocks and established geometric and mathematical models of hydraulic fracture propagation using a 3D meshless method. Obeysekara et al. (2018) proposed a novel approach to modeling fractured rocks by linking a finite discrete element solid model with a control-volume finite element fluid model and validated it against analytical solutions for single-phase flow. Dalla and Picano (2020) proposed a new method for a direct numerical simulation based on the Navier–Stokes equations coupled with the peridynamic theory of solid mechanics and reproduced the fractures in a solid structure under laminar flow conditions.

Many researchers have conducted experiments to study the relationship between seepage behavior and confining or seepage pressures. Seepage test systems have been developed to conduct laboratory experiments on water seepage (Zhang et al. 2021). Cheng et al. (2017) performed experiments on the failure mechanism and seepage behavior of granite under different constraints and concluded that a shear fracturing pattern is more likely to form in granite samples under the effect of water pressure, contrary to conventional triaxial compressive results.

Zhao et al. (2021) proposed a dual-medium model that considers the substantial amount of water stored in the fracture network and the high conductivity of major large-scale fractures and explained the coupled seepage damage effect in fractured rock masses. Jiang et al. (2021) revealed the interaction between the temperature and the osmotic pressure through coupled heat–seepage–stress experiments and found that the number of fracture seepage channels increased at high temperatures, resulting in a higher permeability. Yu et al. (2022b) conducted triaxial compression tests under variable osmotic and confining pressures and developed a new damage constitutive model that could better reflect the stress–strain relationship.

Using the numerical simulation analysis method, a model can be established according to specific parameters to more intuitively restore the deformation field and change process of seepage. Currently, many methods are available for simulating problems involving the interaction between water seepage and rock deformation (Guo et al. 2012; Liu and Liu 2021; Zhou et al. 2022). Xiao et al. (2021) numerically analyzed the hydraulic fracturing process in a multilayered fractured oil reservoir based on the finite element method ABAQUS and obtained a linear relationship between the rock depth and the leakage rate. Chu (2021) established a numerical model of a real mine in FLAC^{3D}, and the simulation results showed the dynamic relationship between the overburden stress and pore water pressure in a confined aquifer for mining. Lei et al. (2017) and Lei et al. (2021) combined the discrete fracture network (DFN) to simulate the geometric characteristics, evolution of geological conditions, and hydraulic characteristics of the natural fracture network formed in rocks and established a fully coupled hydraulic model to solve the stress–strain field in fractured porous media. Li and Liu (2021) used COMSOL to restore the failure process of rocks and analyzed the distribution law of the seepage pressure at characteristic points under different coupling conditions. He and Zhuang (2018) and Shi et al. (2021) concluded that the fracture propagation path tends to extend toward pressurized pores and is significantly affected by existing pressurized pores and the basic properties of porous media.

More studies should be conducted to explain the seepage laws of water in rocks under the effect of hydromechanical interactions and develop applicable models. Abundant evidence has indicated that the behavior of water seepage is affected by the deformation and stress of rocks. However, systematic experimental verification of the effects of external load (such as the axle pressure and confining pressure) and pore water pressure on permeability are relatively lacking. Hence, this study conducted mathematical modeling and simulations based on the effective stress. An effective stress-sensitive permeability model was established, with two sets of seepage experiments conducted to validate the model. A fully coupled multifield model of water seepage and rock deformation was established, and a scenario-based numerical simulation was conducted. The modeling and simulation results of this study can provide insights into the water seepage behavior of rocks under the effect of hydromechanical interactions.

2 Permeability Model Based on Effective Stress

2.1 Modified Permeability Model with Effective Stress

Seepage in a rock mass is generally believed to obey Darcy's law, in which the mean permeability of rock samples in a seepage experiment is often calculated using the following equation:

$$k = \frac{\mu HV}{C\Delta p\Delta t} \quad (1)$$

where k is the permeability of the rock sample, m^2 . V is the inflow volume of the seepage water in unit time, m^3 . μ is the dynamic viscosity of water (Pa s). H and C are the height and cross-sectional area of the rock samples, m , m^2 , respectively. Δt is the time increment, s . Δp is the increment in the water pressure, defined as $\Delta p = p_2 - p_1$, where p_2 and p_1 are the water pressures at the injection inlet and outlet, respectively, in the experiments (MPa).

A rock can be considered a complex porous medium that is often idealized as a dual-porosity medium comprising a matrix and a fracture system. Its permeability is mainly related to the fracture system because the pores in a rock matrix have a significantly lower porosity than the fractures. Consequently, the flow velocity of the water in the fracture system will be greater than that in the rock matrix.

The fractures in a rock are mostly layered structures, and the permeability and porosity φ of the rock mass can be expressed as (Zhang et al 2023):

$$k = \frac{L}{12\tau} b^3 \quad (2)$$

$$\varphi = bS \quad (3)$$

where the equivalent aperture of the layered fracture is b , the average tortuosity is τ , the fracture length per unit cross section is L , and the fracture area per unit volume is S .

Combining Eqs. (2) and (3), the permeability of the rock mass can be expressed as:

$$k = \frac{L}{12\tau S^3} \varphi^3 \quad (4)$$

Because the porosity varies with the deformation, the deformation is governed by the stress tensor σ_{ij} which represents the internal stress that is purely caused by the external load of the rock sample without considering of pore water pressure. In Eq. (4), the partial derivative of the permeability with respect to the stress can be expressed as:

$$\begin{aligned} \frac{\partial k}{\partial \sigma_{ij}} &= \frac{L\varphi^2}{4\tau S^3} \frac{\partial \varphi}{\partial \sigma_{ij}} = 3D_f k \\ D_f &= \frac{1}{\varphi} \frac{\partial \varphi}{\partial \sigma_{ij}} \end{aligned} \quad (5)$$

where D_f represents the coefficient of the stress effect on the rock porosity. D_f is positively correlated with the rock mass damage D as (Teng et al. 2019):

$$D_f = \lambda_f D \quad (6)$$

where λ_f is the sensitivity coefficient of the fracture development with respect to the change in the stress.

Based on the compression characteristics of porous materials, the sensitivity coefficient λ_f can be expressed using the rock mass compression coefficient c_f as follows:

$$\lambda_f = -\lambda_k c_f \quad (7)$$

where λ_k represents the influence coefficient of damage on rock permeability.

By substituting the damage variable and compression coefficient of the rock mass into Eq. (5), we obtain:

$$\frac{\partial k}{\partial \sigma_{ij}} = -3\lambda_k c_f D k \tag{8}$$

By integrating Eq. (8), we can describe the coevolution of the permeability, stress, and damage to the rock mass as follows:

$$k = k_0 e^{-3\lambda_k c_f D(\sigma_{ij} - \sigma_{ij0})} \tag{9}$$

where the subscript “0” represents the initial values of the corresponding variables.

When considering the action of water pressure, the effective stress on the rock skeleton should include the components of the external stress tensor σ_{ij} and water pressure p , which are further denoted by

$$\sigma'_{ij} = \sigma_{ij} - \alpha p \tag{10}$$

Here, σ'_{ij} is the effective stress tensor acting on the solid skeleton (MPa), and α is the Biot’s coefficient.

After substituting Eq. (10) into Eq. (9), the rock permeability in Eq. (9) can be modified into an effective stress-sensitive form as follows:

$$k = k_0 e^{-3\lambda_k c_f D[(\sigma_{ij} - \alpha p) - (\sigma_{ij0} - \alpha p_0)]} \tag{11}$$

From Eq. (11), the rock permeability and effective stress have a negative exponential relationship, which can be further expressed as:

$$k = k_0 e^{-A\sigma_{ij} + Bp} \tag{12}$$

where A is the stress influence coefficient, and B is the pore water pressure influence coefficient.

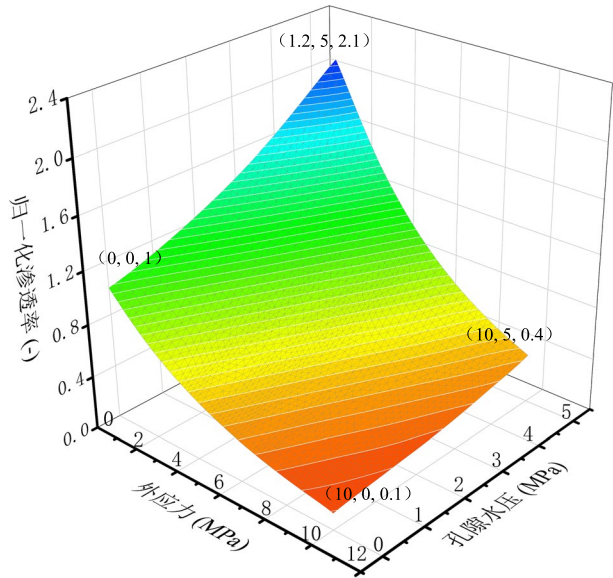
Figure 1 shows the evolution of the normalized permeability k/k_0 with the effective stress, including the external stress and pore water pressure. This indicates that a higher water pressure corresponds to a higher rock permeability, whereas a higher external stress corresponds to a lower permeability.

2.2 Validation of Permeability Model by Experiments

2.2.1 Experimental Program

In this section, two sets of experiments, denoted by A and B , are presented to explore the effects of the pore water pressure and external stress, at the Beijing Key Laboratory for Precise Mining of Intergrown Energy and Resources, China University of Mining and Technology, Beijing. For these experiments, rock samples of argillaceous sandstone were obtained from the Buertai coal mine located in the Shendong mining area, China. In accordance with the International Society for Rock Mechanics (ISRM), the samples were processed into cylindrical shapes with a height of 100 mm and a diameter of 50 mm. The density of the used kind of rock samples was $2.34 \times 10^3 \text{ kg/m}^3$. Based on the mercury injection test, the porosity has an average of 5.4%. Before the experiments, naturally dried rock samples were weighed and then placed in a container of pure water for spontaneous

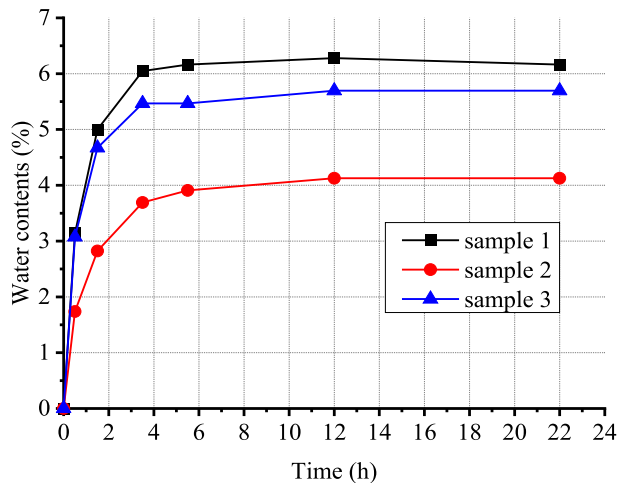
Fig. 1 Evolution of normalized permeability (k/k_0) with external stress and pore water pressure



penetration. We took out the samples and weighed them regularly to calculate the increment in weight until the weight no longer changes, thus rock samples are regarded as natural adsorption saturation. Figure 2 shows the water contents in some of the rock samples during soaking, indicating that the rock sample reaches saturation after soaking for 6 h. The seepage experiments were conducted using a rock stress-seepage-temperature-chemical servo test system, which uses a computer terminal system to control the sample environment (shown in Fig. 3).

In Experiment A, the confining pressures were firstly loaded to 2 and 4 MPa, respectively. Then, the corresponding servo targets of the axial pressure were loaded to 4 and 6 MPa correspondingly. The outlet flow was recorded when the injecting water pressure was increased from 0.1 to 1 MPa, whereas the outlet was connected to the atmospheric

Fig. 2 Temporal variation in the water content in a part of the rock sample



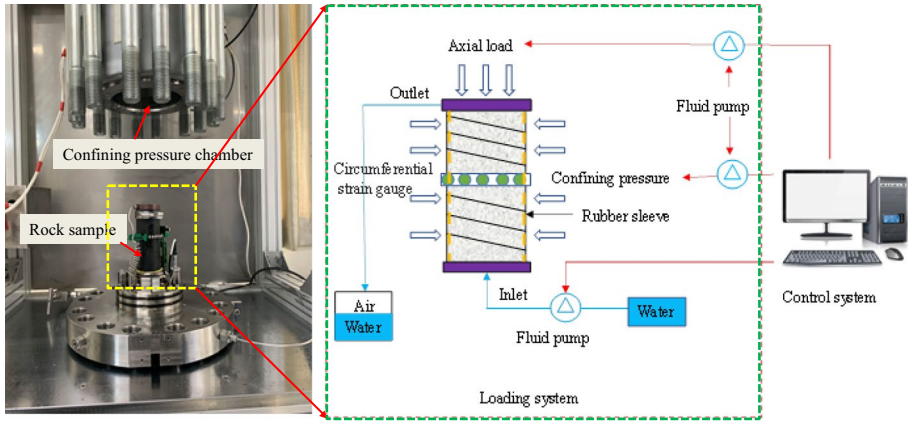


Fig. 3 Triaxial multifield test system for rocks

environment. In Experiment B, the terminal confining pressure keeps 3 MPa. The pressure of the water injected into the inlet was maintained at 2 MPa. The axial compressive stress acting on the rock sample was controlled in a stepwise manner from zero until complete failure. At each step, the deformation speed was maintained at 0.02 mm/min. It is important to note that the flow test was conducted when the axial compressive stress reached the attainment at each step. To ensure the accuracy of the seepage experimental results, the permeability at each step was tested thrice, and the time interval between each test was at least 3 min. All the experimental data mentioned in the following analysis are the mean values.

The external stress in the first set of experiments (A) and water pressure in the second set of experiments (B) were constant. Equation (12) was further improved for application to different experimental data as follows:

$$k = A_1 e^{Bp} \tag{13}$$

and

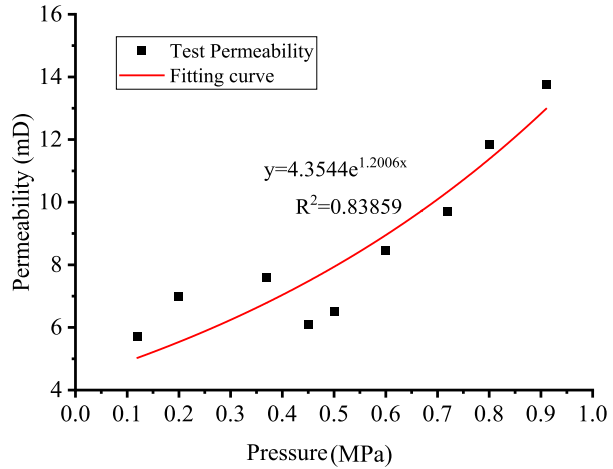
$$k = B_1 e^{-A\sigma_{ij}} \tag{14}$$

where A_1 and B_1 are the seepage parameters.

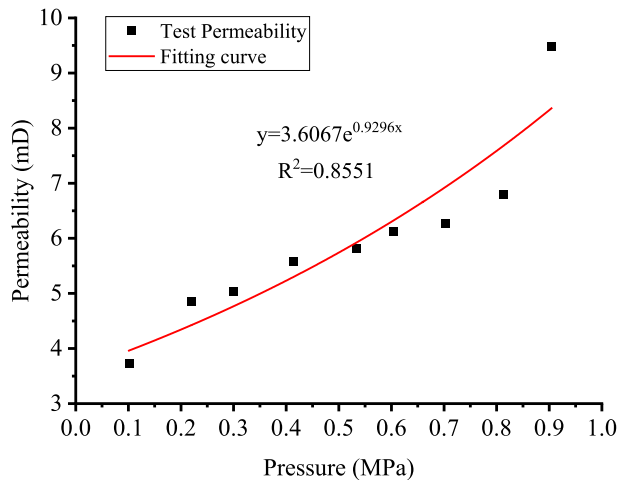
2.2.2 Evolution of Permeability with Water Pressure: Experiment A

Figure 4 present the experimental permeability data of the rock samples in Experiment A and the fitting results with increasing pressure gradient obtained using Eq. (13). The permeability of the rock sample increased exponentially with an increase in the pressure gradient. This is because an increase in the water pressure caused a decrease in the effective stress on the fractures at constant confining and axial pressures. The porosity and permeability increased with increasing aperture of the fractures. The fractures were further compacted with increasing confining pressure, thereby reducing the number of hydrophobic channels and decreasing the permeability. A comparison between Fig. 4a, b shows that the

Fig. 4 Validation of the permeability evolution with different water pressures



(a) Confining pressure: 2 MPa.



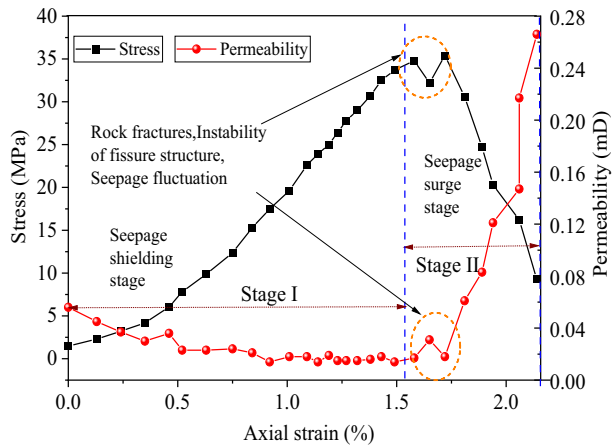
(b) Confining pressure: 4 MPa

permeability of the rock samples is reduced by approximately 30% under the same water pressure with an increase in the confining pressure from 2 to 4 MPa.

2.2.3 Coevolution of the Permeability with Stress and Deformation: Experiment B

Figure 4 shows the coevolution relationship of the permeability with the compressive stress–strain in the entire compression failure process. Figure 5 shows that the trends in the stress–strain and permeability are reversed; the stress–strain curve shows a peak shape, whereas the permeability evolution curve with the axial strain shows a valley shape. The failure corresponding to the extreme strength value can be divided into two stages. The

Fig. 5 Coevolution of the permeability with the compressive deformation



complete evolution of the permeability can be divided into two stages. The first stage is the stress loading stage, which is also the seepage shielding stage. When the stress was increased from 0 to 33.7 MPa, the permeability of the rock sample gradually decreased from an initial value of 0.056–0.014 mD, a decrease of 75%. This is attributed to the increase in the effective stress, which reduces the number of internal seepage fractures and decreases the fracture aperture, making it difficult for the water to penetrate. The second stage is the stress unloading stage in which the stress decreases from the peak value of 34.8 to 9.26 MPa. The second stage is the seepage surge stage. In this stage, the permeability of rock sample increases from 0.014 to 0.27 mD by 3.8 times than it was before, showing an explosive growth with the decrease in the effective stress.

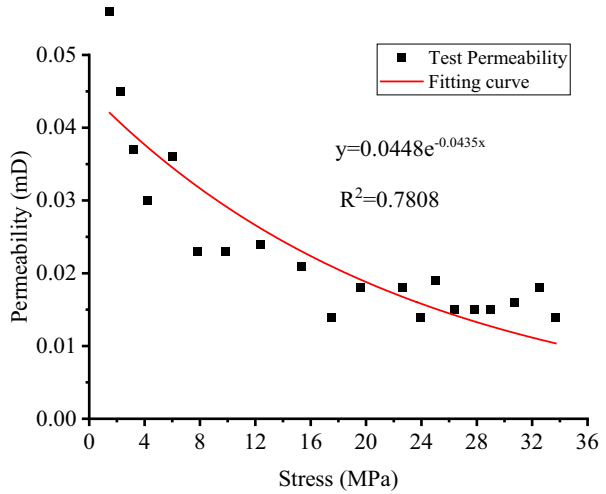
Conventionally, the failure of rock samples is considered to occur as a quantitative change before or at the peak strength, where a large number of cracks appear in the rock sample. Figure 5 shows that the maximum permeability is not consistent with the failure of the rock sample. This was because the newly created fractures were still small and disconnected when the rock sample failed; however, they expanded and combined to form penetrating fractures with further compression in the post-peak stage, resulting in an increase in the fracture aperture and a sudden increase in the permeability. The evolution of permeability with the axial deviatoric stress in stages I and II was validated using Eq. (14), respectively. Satisfactory results were obtained from the fitting results, as shown in Fig. 6.

3 Modeling the Multifield Coupling Between Water Seepage and Rock Deformation

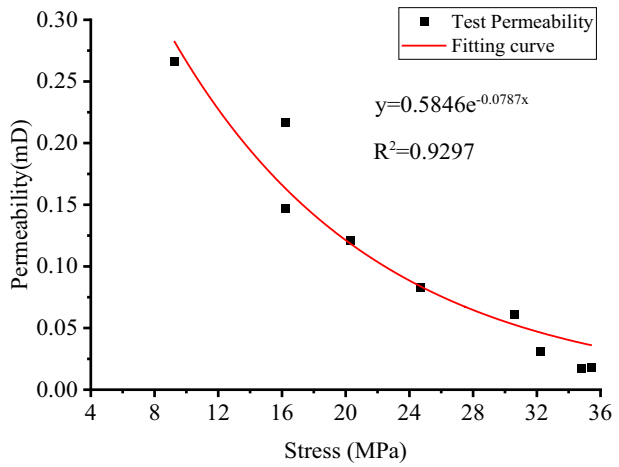
3.1 Porosity Model

Natural rocks have abundant fractures of different sizes, and the porosity is often used to express the cumulative quantity of fractures. Porosity affects the seepage velocity of water. The basic porosity model is defined as the proportion of the fracture volume in the rock. Various expressions were established under the influence of different loads or conditions. For example, Zheng et al. (2015) considered the porosity of rock and divided it into two components: a hard component φ_e and a soft component φ_i :

Fig. 6 Fitting curves of permeability with stress



(a) Stage I



(b) Stage II

$$\varphi_e = \varphi_{e,0}(1 - C_e\sigma) \tag{15}$$

$$\varphi_t = \gamma_{t,0} \exp\left(-\frac{\sigma}{K_t}\right) \tag{16}$$

where $\varphi_{e,0}$ is the initial porosity of the hard component, and C_e is the compressibility of the hard fraction of the fracture volume. $\gamma_{t,0} = V_{0,t}/V_0$, where $V_{0,t}$ is the volume of the soft part when the stress is zero, and V_0 is the bulk volume of the rock under free conditions.

Considered a rock sample and established a pipeline model, and the porosity was expressed as follows:

$$\varphi = \frac{\pi ab}{S} \tau \tag{17}$$

where a and b are the principal semi-axes of the ellipsoids, m . S is the cross-sectional area, m^2 . Considering the dual-porosity structure of the rock, particularly the pore volume contributed by the matrix, the rock porosity can be written as (Zhang et al. 2021):

$$\varphi = \varphi_0 \exp \left\{ \left(\frac{1}{K} - \frac{1}{K_f} \right) [(\sigma - \sigma_0) + \alpha_m(p_m - p_0) + \alpha_f(p_f - p_0)] \right\} \tag{18}$$

where α_m and α_f represent the Biot’s poroelastic coefficients of the matrix and fracture, respectively.

In this study, it was assumed that the rock mass was a uniform porous elastomer without considering thermal expansion or chemical reactions. The porous medium of a rock is composed of a solid skeleton and fractures. As the porosity of the rock and its changes are relatively low, the porosity expressed in Eq. (18) can be expanded using Taylor’s equation, as follows:

$$\varphi = \varphi_0 + \alpha \left(\varepsilon_v + \frac{p - p_0}{K_s} \right) \tag{19}$$

where φ_0 is the initial porosity, α is the Biot–Willis coefficient, as defined in Eq. (10), ε_v represents the volumetric strain, p_0 represents the initial water pressure (MPa), and K_s represents the solid bulk modulus.

3.2 Governing Equation for Rock Deformation

The effective stress of an isotropic porous rock can be expressed using Hooke’s law.

$$\sigma'_{ij} = \lambda \varepsilon_v \delta_{ij} + 2G \varepsilon_{ij} \tag{20}$$

where λ and G are the Lamé constants of the porous media, ε_v is the volumetric strain of the rock, and δ_{ij} denotes the Kronecker symbol (if $i \neq j$, $\delta_{ij} = 0$, and $\delta_{ij} = 1$ when $i = j$).

According to the elasticity theory, the volumetric strain is the accumulation of the normal strains in the x , y , and z directions as follows:

$$\varepsilon_v = \nabla \cdot \overline{W} = \frac{\partial W_x}{\partial x} + \frac{\partial W_y}{\partial y} + \frac{\partial W_z}{\partial z} \tag{21}$$

where W_x , W_y , and W_z are the displacements of the solid skeleton in the space coordinate system (m).

The strain was derived from the displacement using the geometric equations expressed in Eq. (22).

$$\varepsilon_{ij} = \frac{1}{2} (W_{j,i} + W_{i,j}) \quad (22)$$

The balance equation for the elastic material is as follows:

$$\sigma_{ij} + F_i = 0 \quad (23)$$

where F_i represents the body force, MPa.

Thus, the satisfied static balance equation for the internal stress and water pressure in the rock can be expressed as:

$$\sigma_{ij} + \alpha p \delta_{ij} + F_i = 0 \quad (24)$$

3.3 Governing Equation for Water Seepage

According to the law of mass conservation, the mass of water flowing into a rock is equal to the mass of water flowing out. The general mass balance equation for water is expressed as:

$$\frac{\partial m}{\partial t} + \nabla \cdot (\rho_1 \cdot \mathbf{v}) = 0 \quad (25)$$

where ρ_1 is the density of water, kg/m^3 . $m = \rho_1 \varphi$ represents the mass of water per unit volume of rock (kg). t represents time (s), and $\mathbf{v} = -k/\mu \cdot \nabla p$ is the velocity of water, which is assumed to obey Darcy's law (m/s).

The density of water under isothermal conditions is generally expressed using the water pressure as (Du et al. 2018):

$$\rho_1 = \rho_0 e^{[(p-p_0)/K_1]} \quad (26)$$

where ρ_0 is the initial density of the water, kg/m^3 . K_1 is the bulk compressive modulus in Pa.

Taking logarithmic operations on both sides of Eq. (26) and taking the derivative with respect to time t , we obtain:

$$\frac{1}{\rho_1} \frac{\partial \rho_1}{\partial t} = \frac{1}{K_1} \frac{\partial p}{\partial t} \quad (27)$$

By substituting Eqs. (26) and (27) into Eq. (25) and simplifying the water seepage-controlling equation under hydromechanical coupling in a porous rock, we can obtain the following differential equation satisfying the pore water pressure with the validated stress-sensitive permeability model as:

$$-\nabla \cdot \left(\rho_1 \cdot \frac{k}{\mu} \nabla p \right) + \rho_1 \left(\frac{\alpha}{K_s} + \frac{\varphi}{K_1} \right) \frac{\partial p}{\partial t} + \alpha \rho_1 \frac{\partial \varepsilon_v}{\partial t} = 0 \quad (28)$$

4 Program of Numerical Experiment

For further analysis, the mathematical models expressed in Eqs. (24) and (28) were substituted into the finite element simulation software COMSOL for a numerical simulation. A numerical experimental program is described in this section.

4.1 Establishment of a Geometric Model

The numerical model was designed in the form of a cylinder with the same geometric size as the samples used in the experiments described in Sect. 2. The diameter and height were 50 mm and 100 mm, respectively. A linear elastic material was set as the numerical material. The origin of the coordinates was at the center of the bottom surface of the argillaceous sandstone sample. Figure 7a shows the 3D geometric model generated by the physics-controlled mesh. The total number of free tetrahedral elements was 21,078.

4.2 Setting of Initial Conditions

Considering the actual loading process, experimentally observed data, and fitting results of the physical experiment, the confining pressure environment of the model was determined to be 5 MPa, the axial pressure was 2 MPa, and the injection water pressure was 1 MPa, as shown in Fig. 7b. The surface of the cylinder was set as a no-flux boundary, while water flows in from the lower bottom surface and flows out from the upper top surface. The time calculation length was in the range of 0–30 s, and a transient solver was used. Table 1 lists the parameters used in numerical experiments. The evolutions of the water density, porosity, and permeability are shown in the derivations in Sects. 2 and 3.

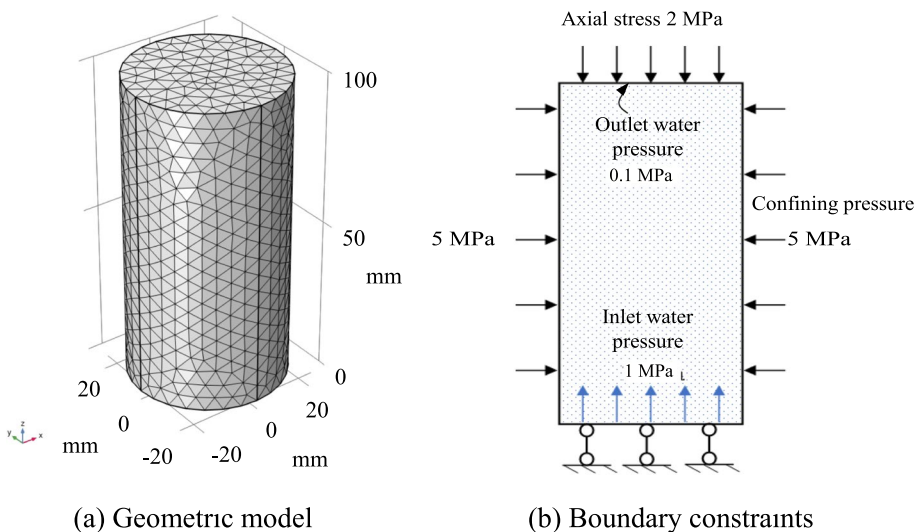


Fig. 7 Geometric model

Table 1 Parameters of argillaceous sandstone used for numerical experiment

Variable	Parameter	Value used	Data sources
ρ_0	Initial density of water (kg/m ³)	1000	Conventional value
μ	Hydrodynamic viscosity (Pa s)	0.001	Conventional value
K_1	Bulk modulus of water (Pa)	2.2×10^9	Conventional value
K_s	Matrix bulk modulus of rock (Pa)	1.76×10^9	Guo et al. (2021)
ρ_s	Matrix density of rock (kg/m ³)	2340	Xiao et al. (2021)
E	Young's modulus of rock (Pa)	2.75×10^9	Guo et al. (2021)
ν	Poisson's ratio	0.24	Guo et al. (2021)
φ_0	initial porosity	0.05	Mercury-injection test
κ_0	Initial permeability (m ²)	5.76×10^{-15}	Experiment (Fig. 4)
λ	Stress factor (Pa ⁻¹)	0.048	Zhao et al. (2021)
α	Biot's coefficient (Pa ⁻¹)	1	Zhao et al. (2021)

5 Analysis of Simulation Results

5.1 Evolution of Water Pressure

The numerical results showed that the change in the water pressure distribution in the argillaceous sandstone sample diminished over time. From the contours of the water pressure after different seepage times shown in Fig. 8, the water pressure distributions changed very little between seepage times of 20 and 30 s (Fig. 8e, f); thus, the seepage is considered to reach an equilibrium distribution in the sample after 30 s. The observation time points in the following analysis are 0.05, 1, 5, 10, 20, and 30 s, varying from the beginning to the final equilibrium of seepage. Figure 9 compares the water pressure with the flow distance from the inlet at the observed seepage times. As shown in Figs. 8 and 9, the water pressure exhibits a layered distribution. The higher pressure of water at the initial time was mainly limited to the injection inlet of the sample, and this position gradually extended upward before seepage equilibrium was reached.

5.2 Deformation of Argillaceous Sandstone Sample

Figure 10 shows the deformation of the rock sample under the combined effect of the water pressure, axial pressure, and confining pressure. Considering the structural symmetry in the x - and y -directions, the strains in the x - and y -directions are identical to those shown in Fig. 10a, and the strain in the z -direction is shown in Fig. 10b. Because the initial compression strain induced by the axial and confining pressures was higher than the expansion strain induced by the water pressure, the strain values were negative, as shown in Fig. 10. The strains of the sample in the three directions exhibited similar evolution trends. The increase in the internal water pressure offsets the compressive deformation of the external loading to a certain degree. Thus, the strains increased with increasing distance from the inlet surface and decreased when the seepage pressure approached equilibrium.

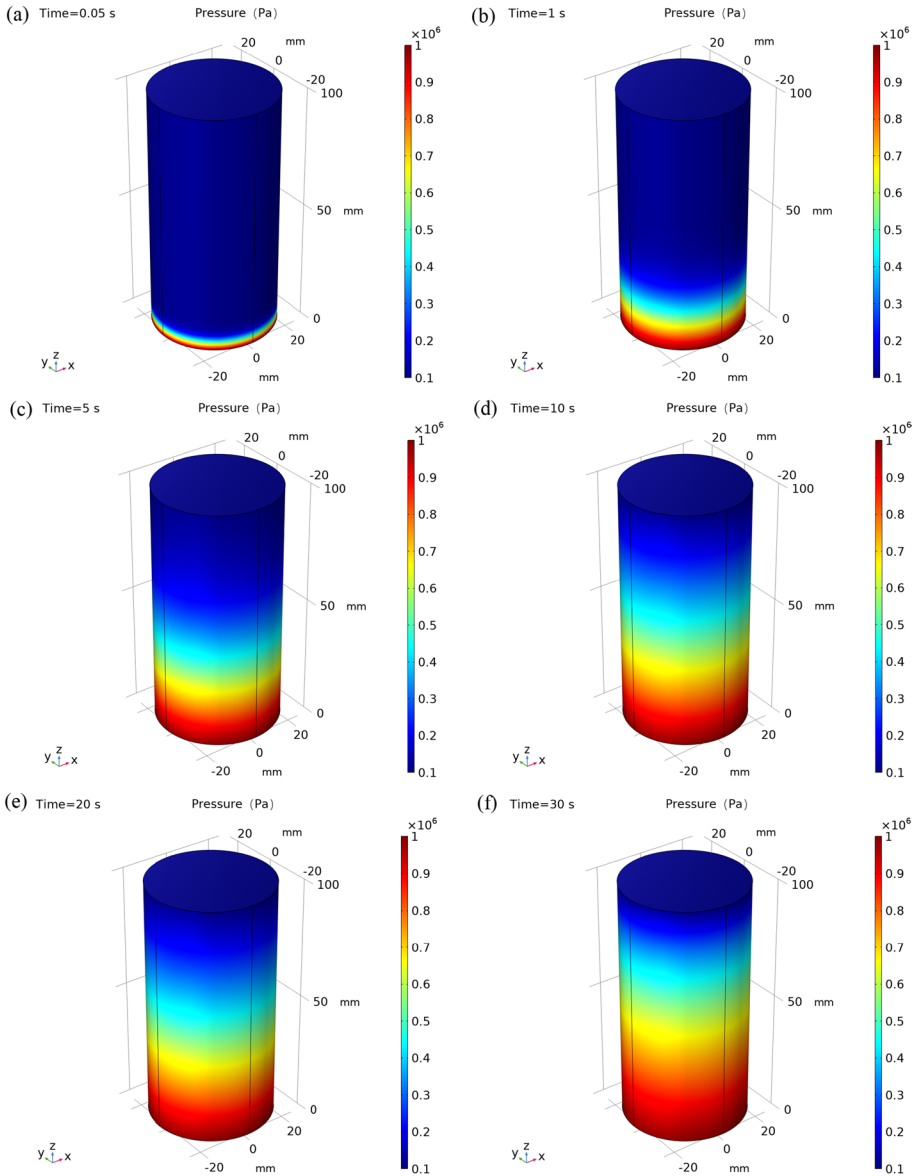


Fig. 8 Contours of the water pressure after different times

5.3 Evolution of Permeability

Six observation points were selected from the z-direction centerline of the sample with flow distances of 0, 20, 40, 60, 80, and 100 mm. Figure 11 shows the evolution of the permeability at these observation positions with time. As shown, the increasing tendency in the permeability decreases with seepage time, except at positions with distances of 0 mm and 100 mm of constant initial values, which correspond to the seepage inlet and

Fig. 9 Evolution of the water pressure with flow distance from inlet

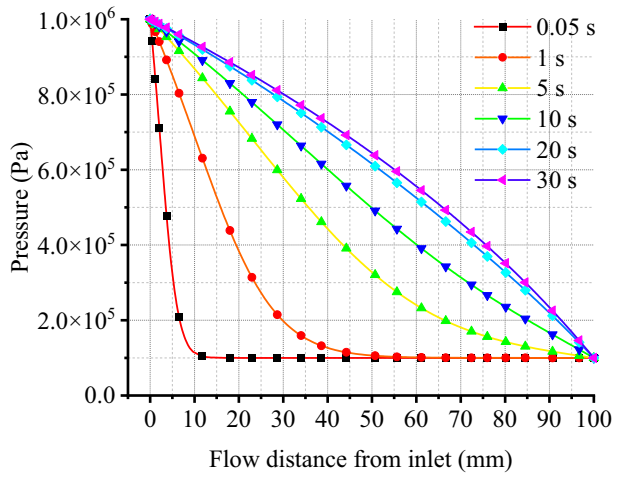
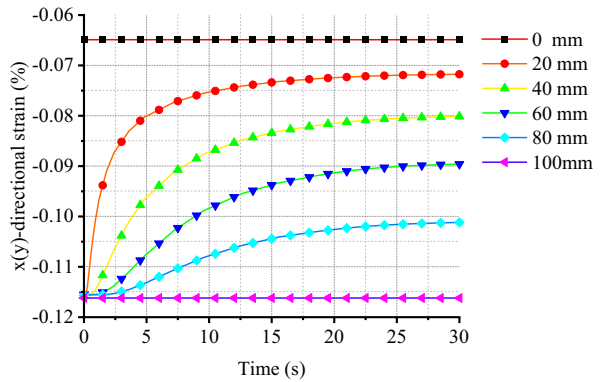
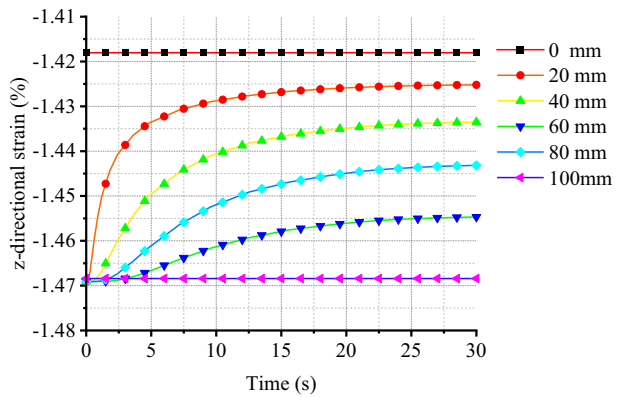


Fig. 10 Composite deformation of rock sample

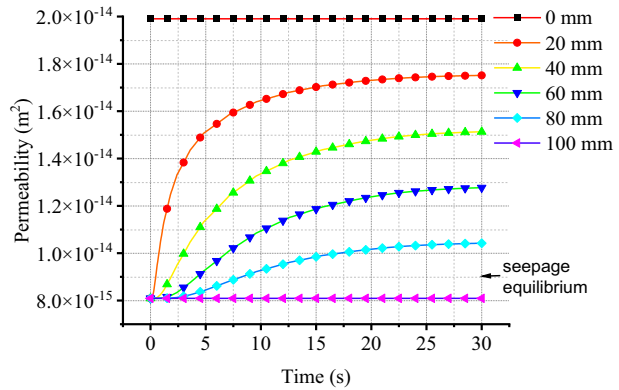


(a) Strain in the x- and y-directions



(b) Strain in the z-direction

Fig. 11 Evolution of permeability at different distances from the inlet



outlet surfaces controlled by the boundary conditions. Taking the 20 mm position as an example, we found that the permeability doubled from its initial value of $0.8 \times 10^{-14} \text{ m}^2$ in the first 10 s of seepage and increased by only 12% in the later 20 s. The permeability at each observation point did not increase when the water seepage reached equilibrium after approximately 30 s. The influence of the boundary stress and pore water pressure on the permeability governed by Eq. (12) remained unchanged after reaching equilibrium.

6 Conclusions

This study developed a mathematical effective stress-sensitive permeability model for argillaceous sandstone under coupled hydromechanical conditions. Two sets of seepage experiments were conducted to validate the proposed stress-sensitive permeability model by controlling the water pressure and external stress, respectively. Based on the proposed permeability model, a fully coupled multifield model for water seepage and rock deformation was established. Subsequently, a scenario-based numerical simulation in a finite element environment was conducted to investigate the evolutions of the water seepage and rock deformation. The following conclusions can be drawn based on the modeling and simulation results:

1. The permeability and effective stress of the argillaceous sandstone exhibited a negative exponential relationship. A higher water pressure corresponded to a higher permeability, whereas a higher external stress corresponded to a lower permeability.
2. The trends in the evolution of the entire compressive stress–strain and permeability curves were reversed; the stress–strain curve showed a peak shape, whereas the permeability evolution curve showed a valley shape. The maximum value of the permeability was not consistent with the failure of argillaceous sandstone.
3. The water pressure formed a layered distribution. The higher pressure of water at the initial time mainly limited to the injection inlet of the sample, and gradually extended upward before reaching seepage equilibrium.

The modeling and simulation results of this study provide insights into the water seepage characteristics of argillaceous sandstone under hydromechanical interactions. These

insights may be helpful for the development of coupled water–rock mechanics in geotechnical engineering.

Acknowledgements This work was financially supported by the National Natural Science Foundation (52004285), National Key R&D Program of China (2022YFC3004600), Fundamental Research Funds for the Central Universities from China University of Mining and Technology-Beijing (JCCXXNY06), Open Fund of State Key Laboratory Cultivation Base for Gas Geology and Gas Control (Henan Polytechnic University) (WS2021A03), and Open Fund of State Key Laboratory for Geomechanics and Deep Underground Engineering (SKLGDUEK2123).

Author Contributions All authors contributed to the study conception and design. Material preparation, data collection and analysis were performed by YW, ZL and KL. WJ is responsible for data visualization. The first draft of the manuscript was written by TT and all authors commented on previous versions of the manuscript. All authors read and approved the final manuscript.

Declarations

Conflict of interest The authors declare that they have no competing financial interests or personal relationships that could have appeared to influence the work reported in this paper.

References

- Andreas, H., Espen, J., Jens, F., Paul, M., Anders, M.S.: A node-splitting discrete element model for fluid–structure interaction. *Physica A* **416**, 61–79 (2014)
- Biot, M.A.: General theory of three dimensional consolidation. *J. Appl. Phys.* **12**, 155–164 (1941)
- Biot, M.A., Willis, D.G.: The elastic coefficients of the theory of consolidation. *ASME J. Appl. Mech.* **24**, 594–601 (1957)
- Chen, L.W., Ou, Q.H., Peng, Z.H., Wang, Y.X., Chen, Y.F., Tian, Y.: Numerical simulation of abnormal roof water-inrush mechanism in mining under unconsolidated aquifer based on overburden dynamic damage. *Eng. Fail. Anal.* **133**, 106005 (2022)
- Cheng, C., Li, X., Li, S.D., Zheng, B.: Failure behavior of granite affected by confinement and water pressure and its influence on the seepage behavior by laboratory experiments. *Materials* **10**, 798 (2017)
- Chu, C.C.: Investigation on the responses of overburden stress and water pressure to mining under the reverse fault. *Geofluids* (2021). <https://doi.org/10.1155/2021/5199755>
- Dalla, B.F., Picano, F.: A novel approach for direct numerical simulation of hydraulic fracture problems. *Flow Turbul. Combust.* **105**, 335–357 (2020)
- Du Xin, Lu.Z.W., Li, D.M., Xu, Y.D., Li, P.C., Lu, D.T.: A novel analytical well test model for fractured vuggy carbonate reservoirs considering the coupling between oil flow and wave propagation. *J. Petrol. Sci. Eng.* **173**, 447–461 (2018)
- Fan, J., Dou, L.M., He, H., Du, T.T., Zhang, S.B., Gui, B., Sun, X.L.: Directional hydraulic fracturing to control hard-roof rockburst in coal mines. *Int. J. Min. Sci. Technol.* **22**(2), 177–181 (2012)
- Golovin, S.V., Baykin, A.N.: Influence of pore pressure to the development of a hydraulic fracture in poroelastic medium. *Int. J. Rock Mech. Min.* **108**, 198–208 (2018)
- Guo, H.Y., He, M.C., Sun, C.H., Li, B., Zhang, F.: Hydrophilic and strength-softening characteristics of calcareous shale in deep mines. *J. Rock Mech. Geotech.* **4**(4), 344–435 (2012)
- Guo, T.K., Zhang, S.Z., Qu, Z.Q., Zhou, T., Xiao, Y.S., Gao, J.: Experimental study of hydraulic fracturing for shale by stimulated reservoir volume. *Fuel* **128**, 373–380 (2014)
- Guo, J.T., Teng, T., Zhu, X.Y., Wang, Y.M., Li, Z.L., Tan, Y.: Characterization and modeling study on softening and seepage behavior of weakly cemented sandy mudstone after water injection. *Geofluids* **2021**, 7799041 (2021)
- Hadi, F., Homayoon, K.: New empirical model to evaluate groundwater flow into circular tunnel using multiple regression analysis. *Int. J. Min. Sci. Technol.* **27**, 415–421 (2017)
- He, B., Zhuang, X.Y.: Modeling hydraulic cracks and inclusion interaction using XFEM. *Undergr. Space* **3**, 218–228 (2018)
- He, H., Dou, L.M., Fan, J., Xu, T.T., Sun, X.L.: Deep-hole directional fracturing of thick hard roof for rockburst prevention. *Tunn. Undergr. Space Technol.* **32**, 34–43 (2012)

- Jiang, H.P., Jiang, A.N., Zhang, F.R.: Experimental investigation on the evolution of damage and seepage characteristics for red sandstone under thermal–mechanical coupling conditions. *Environ. Earth Sci.* **80**, 816 (2021)
- Kacimov, A.R., Obnosov, Y.V., Šimůnek, J.: Seepage to staggered tunnels and subterranean cavities: analytical and HYDRUS modeling. *Adv. Water Resour.* **164**, 104182 (2022)
- Lei, Q.H., Latham, J.P., Tsang, C.F.: The use of discrete fracture networks for modelling coupled geomechanical and hydrological behaviour of fractured rocks. *Comput. Geotech.* **85**, 151–176 (2017)
- Lei, Q.H., Doonechaly, N.G., Tsang, C.F.: Modelling fluid injection-induced fracture activation, damage growth, seismicity occurrence and connectivity change in naturally fractured rocks. *Int. J. Rock Mech. Min.* **138**, 104598 (2021)
- Li, M., Liu, X.S.: Experimental and numerical investigation of the failure mechanism and permeability evolution of sandstone based on hydro-mechanical coupling. *J. Nat. Gas Sci. Eng.* **95**, 104240 (2021)
- Li, Q., Lian, J.J., Zhao, G.F.: A three-phase coupled numerical model for the hydraulic fracturing of rock. *Int. J. Rock Mech. Min.* **152**, 105075 (2022)
- Liu, A., Liu, S.M.: A fully-coupled water-vapor flow and rock deformation/damage model for shale and coal: its application for mine stability evaluation. *Int. J. Rock Mech. Min.* **146**, 104880 (2021)
- Lu, C.P., Dou, L.M., Zhang, N., Xue, J.H., Wang, X.N.: Microseismic frequency-spectrum evolutionary rule of rockburst triggered by roof fall. *Int. J. Rock Mech. Min.* **64**, 6–16 (2013)
- Obeyesekere, A., Lei, Q., Salinas, P., Pavlidis, D., Xiang, J., Latham, J.P., Pain, C.C.: Modelling stress-dependent single and multi-phase flows in fractured porous media based on an immersed-body method with mesh adaptivity. *Comput. Geotech.* **103**, 229–241 (2018)
- Pan, C., Xia, B.W., Zuo, Y.J., Yu, B., Ou, C.N.: Mechanism and control technology of strong ground pressure behaviour induced by high-position hard roofs in extra-thick coal seam mining. *Int. J. Min. Sci. Technol.* **32**, 499–511 (2022)
- Shi, F., Wang, D.B., Chen, X.G.: A numerical study on the propagation mechanisms of hydraulic fractures in fracture-cavity carbonate reservoirs. *CMES-Comper. Model Eng.* **127**, 2 (2021)
- Teng, T., Wang, W., Zhan, P.F.: Evaluation criterion and index for the efficiency of thermal stimulation to dual coal permeability. *J. Nat. Gas Sci. Eng.* **68**, 102899 (2019)
- Terzaghi, K.: *Theoretical Soil Mechanics*, pp. 4–10. Wiley, New York (1943)
- Wen, G.J., Liu, H.J., Huang, H.B., Wang, Y.D., Shi, X.Y.: Meshless method simulation and experimental investigation of crack propagation of CBM hydraulic fracturing. *Oil Gas Sci. Technol.* **72**, 73 (2018)
- Xiao, C.Y., Zhang, G.J., Yu, Y.D.: Numerical analysis of hydraulic fracturing processes for multi-layered fractured reservoirs. *Energy Rep.* **7**, 467–471 (2021)
- Yu, M.L., Zuo, J.P., Sun, Y.J., Mi, C.N., Li, Z.D.: Investigation on fracture models and ground pressure distribution of thick hard rock strata including weak interlayer. *Int. J. Min. Sci. Technol.* **32**, 137–153 (2022a)
- Yu, M.Y., Liu, B.G., Chu, Z.F., Sun, J.L., Deng, T.B., Qi, W.: Permeability, deformation characteristics, and damage constitutive model of shale under triaxial hydromechanical coupling. *Bull. Eng. Geol. Environ.* **81**, 85 (2022b)
- Zhang, Q.X., Hou, B., Lin, B.T., Liu, X., Gao, Y.F.: Integration of discrete fracture reconstruction and dual porosity/dual permeability models for gas production analysis in a deformable fractured shale reservoir. *J. Nat. Gas Sci. Eng.* **93**, 104028 (2021)
- Zhang, J., Gao, S., Xiong, W., Ye, L., Liu, H., Zhu, W., Sun, X., Li, X., Zhu, W.: An improved experimental procedure and mathematical model for determining gas-water relative permeability in tight sandstone gas reservoirs. *Geoenergy Sci. Eng.* **221**, 211402 (2023)
- Zhao, Y., Liu, Q., Zhang, C., Liao, J., Lin, H., Wang, Y.: Coupled seepage-damage effect in fractured rock masses: model development and a case study. *Int. J. Rock Mech. Min.* **144**, 104822 (2021)
- Zheng, J.T., Zheng, L.G., Liu, H.H., Ju, Y.: Relationships between permeability, porosity and effective stress for low-permeability sedimentary rock. *Int. J. Rock Mech. Min.* **78**, 304–318 (2015)
- Zhou, G., Wang, C.M., Liu, R.L., Li, S.L., Zhang, Q.T., Liu, Z., Yang, W.Y.: Variations in air humidity and the duration of roof exposure are known to significantly influence the stability of shale roof strata. *Int. J. Rock Mech. Min.* **150**, 105024 (2022)

Publisher's Note Springer Nature remains neutral with regard to jurisdictional claims in published maps and institutional affiliations.

Springer Nature or its licensor (e.g. a society or other partner) holds exclusive rights to this article under a publishing agreement with the author(s) or other rightsholder(s); author self-archiving of the accepted manuscript version of this article is solely governed by the terms of such publishing agreement and applicable law.